

Unsupervised Tissue Classification

Dzung L. Pham,
and Pierre-Louis Bazin
*Laboratory of Medical Image
Computing
Department of Radiology &
Radiological Science
Johns Hopkins University*

12.1	Introduction	209
12.2	Background	209
12.3	Methods	210
	12.3.1 <i>K</i> -means Approach • 12.3.2 EM approach • 12.3.3 Fuzzy Clustering Approach	
12.4	Results	214
	12.4.1 Brainweb Dataset • 12.4.2 IBSR Datasets • 12.4.3 Sensitivity to Scan Protocol	
12.5	Conclusions	218
12.6	References	221

12.1 Introduction

Accurate tissue classification is an important objective in many medical imaging applications such as in the study of anatomical structure, surgical planning, and computer integrated surgery [1]. Tissue classification algorithms have been especially useful in the segmentation of magnetic resonance (MR) brain images, where the excellent soft tissue contrast allows for volumetric quantification of gray matter and white matter structures in healthy and diseased brain anatomy. Methods for performing tissue classification are hindered, however, by multiple imaging artifacts such as noise, intensity inhomogeneities, and partial volume effects. Noise in MR images can induce segmented regions to become disconnected or possess holes. Intensity inhomogeneities, which are caused by nonuniformities in the RF field and other factors [2], produce a shading artifact over the image that can confound intensity-based segmentation methods. Partial volume effects occur where multiple tissues contribute to a single voxel, resulting in a blurring of intensities at tissue boundaries [3].

In this chapter, a general framework for unsupervised (i.e., requiring no training data) tissue classification is presented. Methods derived from the proposed imaging model are robust to both noise and intensity inhomogeneities. Under this framework, we describe algorithms based on traditional pattern recognition techniques: *K*-means clustering, Gaussian clustering via the expectation-maximization (EM) algorithm, and fuzzy clustering. Unlike the *K*-means algorithm, the latter two approaches are capable of producing soft segmentations that can better model partial volume effects. These robust algorithms fully generalize their traditional counterparts. The performance of the various algorithms is compared using both real

and simulated MR images of the brain. Software implementing these tissue classification approaches has also been made freely downloadable from the internet (<http://medic.rad.jhu.edu>).

This chapter is organized as follows. In Section 12.2, current approaches in tissue classification of brain images are reviewed. In Section 12.3, several tissue classification algorithms are derived from a statistical image model. In Section 12.4, the derived algorithms are compared and validated. Finally, in Section 12.5, the properties of the different algorithms are summarized.

12.2 Background

Most automated tissue classification methods in the MR brain image segmentation literature are derived from traditional pattern recognition techniques, particularly statistical supervised and unsupervised classifiers [4, 5]. Supervised classifiers seek to partition a feature space derived from the image using training data with known labels. Unsupervised classifiers or clustering algorithms perform the same function without the need for training data. Supervised methods are capable, in some situations, of superior performance to unsupervised methods because they incorporate additional knowledge from the training data, which can lead to more accurate models. However, generating the training data for a large number of scans can be laborious. In addition, use of the same training set for different populations may lead to biased results that do not fully capture the variability between different subjects. Unsupervised classifiers, on the other hand, generally must employ simpler data models and iteratively fit the model to the data. The algorithms are therefore slower, but the step for obtaining labels for the training data is obviated.

In order to make classifiers more robust to noise in images, a smoothness constraint is typically employed within the segmentation model. In statistical classifiers, a Markov random field (MRF) model that models spatial interactions between neighboring or nearby pixels is frequently used [6]. Such models penalize unlikely configurations from occurring in the segmentation, such as an anatomical structure consisting of a single pixel or voxel. MRFs may be incorporated under a Bayesian prior model within supervised classifiers [7, 8], as well as unsupervised classifiers such as the K-means algorithm [9, 10] and EM algorithm [11–13]. Other classification approaches incorporating MRF models for tissue classification in MR images have also been proposed [14, 15]. Enforcing smoothness within fuzzy classifiers is also possible [16–18].

Numerous approaches have been proposed in the literature for applying classifiers in the presence of intensity inhomogeneity artifacts. Some methods suggest a prefiltering operation that attempts to remove the inhomogeneity prior to actual segmentation [19–26]. While these methods are flexible in that they make no assumptions on the number of tissue classes, methods that *simultaneously* segment the image while estimating the inhomogeneity offer the advantage of being able to use intermediate information gleaned from the classification process. There are two prevailing approaches for modeling inhomogeneities in methods that perform simultaneous correction and classification. The first approach assumes that the mean tissue intensity for each tissue class is spatially varying and independent of one another [9, 14, 27]. The second approach models the inhomogeneities as a multiplicative gain field [12, 28] or additive bias field of the image logarithm [7, 11, 13, 29]. The latter approach has the advantage of being computationally less expensive and may also be used for removing inhomogeneities by simple multiplication of the acquired image by the reciprocal of the estimated gain field (or by subtracting the additive bias field). On the other hand, it has been suggested that RF inhomogeneities may be a tissue-dependent effect [2] and different tissue classes may have some inherent variability, in which case the former model would be more appropriate.

Because of partial volume effects, it is often desirable to allow for some uncertainty in tissue classification. So-called soft segmentations allow multiple tissues to exist at a particular location with different levels of membership or probability. Methods based on the EM algorithm are able to obtain a soft segmentation by computing a posterior probability at each pixel [7, 11, 29]. Fuzzy clustering algorithms are also capable of computing soft segmentations [18, 30]. Partial volume effects may also be explicitly incorporated into the classifier model either by considering separate partial volume tissue classes [3, 26, 31, 32], or by directly estimating partial volume fractions [26, 32–37]. Partial volume segmentation is also addressed in Chapter 13 in this Handbook.

Spatially varying prior probability functions may also be used to enhance the tissue classification algorithm [8, 11].

These methods use training data to encode the probability of a tissue class occurring at a particular spatial location within the image. A registration algorithm is required to align the spatial priors to the image. Efforts to integrate the registration and classification process have also been promising [38–42]. When combined with more detailed spatial priors, these approaches have the ability to segment beyond standard gray matter, white matter, and cerebrospinal fluid (CSF) tissue classes [39, 41]. A somewhat less restrictive constraint than the use of spatial priors is to enforce topological consistency in the resulting classification [43–45].

The framework presented in this chapter shares many similarities with a number of these aforementioned tissue classification approaches, particularly those based on unsupervised classifiers. Although the basic model used is fairly straightforward, it easily extends to incorporate spatial priors, topological constraints, or simultaneous registration. In addition, the described approach may also be used to form the basis for classifying diseased anatomy by considering additional classes or outlier classes (cf. [46]).

12.3 Methods

In this section, we describe the underlying model that will be used for performing tissue classification. The observation model assumes the image is a piecewise constant image that is corrupted by intensity inhomogeneities and noise. A prior probability model is placed on the tissue classes to enforce smoothness in the segmentation. Throughout, the total number of classes is assumed to be known. For notational simplicity, only scalar images are considered, although all the mathematics straightforwardly generalizes to multichannel image data [47].

The true image is assumed to be composed of K tissue classes, with each class having a distinct, unknown, intensity value called the *class mean*, denoted $v_k, k = 1, \dots, K$. Because of intensity inhomogeneities or variability in the tissue itself, the class means may be spatially varying in the image domain Ω . Two cases are considered in regard to this variation. In the more general case, each mean can be considered to vary independently:

$$y_j = \sum_{k=1}^K z_{jk} v_{jk} + \eta_j, \quad j \in \Omega, \quad (12.1)$$

where y_j is the observed intensity at pixel j , and η_j is white Gaussian noise with unknown variance σ^2 . In the second case, which is the focus of this work, each mean varies according to a multiplicative gain field, g_j .

$$y_j = g_j \sum_{k=1}^K z_{jk} v_{jk} + \eta_j, \quad j \in \Omega. \quad (12.2)$$

We define z_{jk} to be indicator functions that satisfy

$$z_{jk} = \begin{cases} 1, & \text{if pixel } j \text{ is in tissue class } k \\ 0, & \text{otherwise,} \end{cases} \quad (12.3)$$

and $\sum_{k=1}^K z_{jk} = 1$ (i.e., classes do not overlap). Thus, a segmentation can be obtained by estimating the indicator functions. This model for the true image appears similar to models used in partial volume estimation [3, 31, 33]. The primary difference in the partial volume estimation models is that they allow the indicator functions to take on values between 0 and 1, while here, the indicator functions are binary-valued. However, in Section 12.3.2, it will be shown that if the problem is posed in an EM framework, expectations of z_{jk} are computed, allowing it to take on values between 0 and 1. These estimates of z_{jk} can be interpreted as measures of partial volume. Furthermore, a fuzzy clustering interpretation will also allow modeling of partial volume effects.

Given the observation model of Equation 12.2, the likelihood function can be expressed as

$$f(y; z, \theta) = \prod_{j \in \Omega} \frac{1}{\sqrt{2\pi\sigma^2}} \exp\left(-\left(y_j - g_j \sum_{i=1}^K z_{jk} v_k\right)^2 / 2\sigma^2\right), \quad (12.4)$$

where \mathbf{y} represent stacked vectors, and θ is the parameter vector consisting of the means, variance, and gain field. In order to make our model more robust to noise and intensity inhomogeneities, we employ a Bayesian estimation framework: given the observed image \mathbf{y} , determine the most probable indicator functions and parameters. Prior probability functions are placed on the indicator functions so that the tissue classes form connected regions. In addition, a prior may also be placed on the spatially varying means or the gain field, to enforce the assumption that the inhomogeneity effects are smooth and slowly varying [7, 30, 48]. Alternatively, these properties can also be enforced by representing the gain field as a summation of smooth basis functions (e.g., splines, polynomials) [11, 26].

A Markov random field prior model is used for the indicator functions z_{jk} [49] that discourages the formation of regions consisting of disconnected pixels and is given by

$$f(z) = \frac{1}{Z_z} \prod_{j \in \Omega} \exp\left(-\beta \sum_{i \in N_j} z_j^T V z_i\right), \quad (12.5)$$

where β is a parameter controlling the strength of the prior and is determined empirically, N_j is the set of the four nearest neighbors of j for 2D images and six nearest neighbors for 3D images, and Z_z is a normalizing constant. The matrix \mathbf{V} is $K \times K$ and is used to penalize the classification of pixel j based on its neighbors. In this work, $V = [1, \dots, 1][1, \dots, 1]^T - I$, where I is the $K \times K$ identity matrix. Thus, a pixel belonging to the same tissue class as its neighbors is favored over configurations consisting of different classes.

12.3.1 K-means Approach

One approach for estimating an optimal segmentation under the given model is closely related to the K -means (or ISODATA) algorithm [4]. Maximization of the joint posterior probability function is equivalent to minimizing the following sum of two energy functions:

$$E = \frac{1}{2\sigma^2} E_1 + \beta E_2. \quad (12.6)$$

The first term represents a data term:

$$E_1 = \sum_{j \in \Omega} \sum_{k=1}^K z_{jk} (y_j - g_j v_k)^2.$$

The second term is a Markov random field term that enforces continuity within the indicator functions:

$$E_2 = \sum_{j \in \Omega} \sum_{i \in N_j} z_j^T V z_i.$$

The equation for E_1 follows from the properties that $z_{jk}^2 = z_{jk}$ and $\sum_{k=1}^K z_{jk} = 1$. Except for the gain field term, E_1 is exactly the K -means clustering algorithm objective function. Minimization of E is therefore equivalent to a penalized K -means algorithm and can be solved using an iterative approach. Without loss of generality, we ignore the effects of σ^2 , since its value merely influences the balance of the different energy functions.

Similar to the standard K -means algorithm, a coordinate descent optimization is used that first estimates the indicator functions, then the means of each class, then the gain field, and iterates between these three steps. To estimate the indicator functions, we perform the following computation for each pixel $j \in \Omega$:

$$z_j = \arg \min_{z_j} \left[(y_j - g_j \sum_{k=1}^K z_{jk} v_k)^2 + \lambda \sum_{i \in N_j} z_j^T V z_i \right]. \quad (12.7)$$

This step is similar to the iterated conditional modes algorithm [49]. The estimation of the means can be derived by solving for a zero gradient of Equation 12.6 with respect to each mean:

$$v_k = \frac{\sum_{j \in \Omega} z_{jk} g_j y_j}{\sum_{j \in \Omega} z_{jk} (g_j^2)}. \quad (12.8)$$

When g_j is unity, Equation 12.8 is identical to the computation of the means in the standard K -means algorithm.

We make the simplifying assumption that the gain field g can be represented by a low-degree three-dimensional polynomial function. Although this assumption is somewhat more

restrictive than that of [30], it is usually sufficient to model the intensity variations (cf. [11]), is computationally more efficient, and requires fewer initial parameters to be specified. Mathematically, the gain field can be expressed as

$$g_j = \sum_{n=1}^N f_n P_n(j),$$

where P_n are polynomial basis functions and f_n are the coefficients. We use Chebyshev polynomial basis functions for their numerical stability and other advantageous properties for function approximation [50]. The number of Chebyshev coefficients are 20 for the 3rd degree case, and 35 for 4th degree polynomial fields. Because the gain field is assumed to be smooth and the equations are overdetermined, we subsample the images by a factor of 3 along each dimension when computing the coefficients f_n to increase the computational efficiency.

The complete iterative algorithm, which we call the robust K -means algorithm, can be stated as follows:

Algorithm: Inhomogeneity and Noise Robust K -means

1. Obtain initial estimates of the centroids, \mathbf{v}_k , and assume $g_j = 1$.
2. Solve for indicator functions using Equation 12.7.
3. Solve for means using Equation 12.8.
4. Solve for gain field by solving the following matrix equation for the coefficients f_n :

$$[z_{jk} v_k P_n(j)] \cdot [f_n] = [z_{jk} y_j]. \quad (12.9)$$

5. Go to step 2 and repeat until convergence.

Initial estimates of the means may be obtained by using random guesses, partitioning the intensity space, or by determining the modes of the histogram [12]. Convergence is typically assumed to be achieved either when the classification has minimal changes between iterations or when the changes in the cost function between iterations are below some threshold.

Figure 12.1 shows the results of applying the robust K -means algorithm to a T1-weighted magnetic resonance image of the brain. The image was acquired on a General Electric 1.5T scanner using a Spoiled Gradient Recall (SPGR) protocol. The brain image was preprocessed to extract the cerebral tissue. A slice of the image is shown in Figure 12.1a. Three tissue classes, corresponding to gray matter (GM), white matter (WM), and CSF were assumed to be present within the image. Background pixels were ignored. The algorithm outputs indicator functions for each tissue class, shown in Figures 12.1c–e, as well the estimated inhomogeneity field shown in Figure 12.1f. The indicator functions are summarized in Figure 12.1b where dark gray represents CSF, medium gray represents GM, and white represents WM.

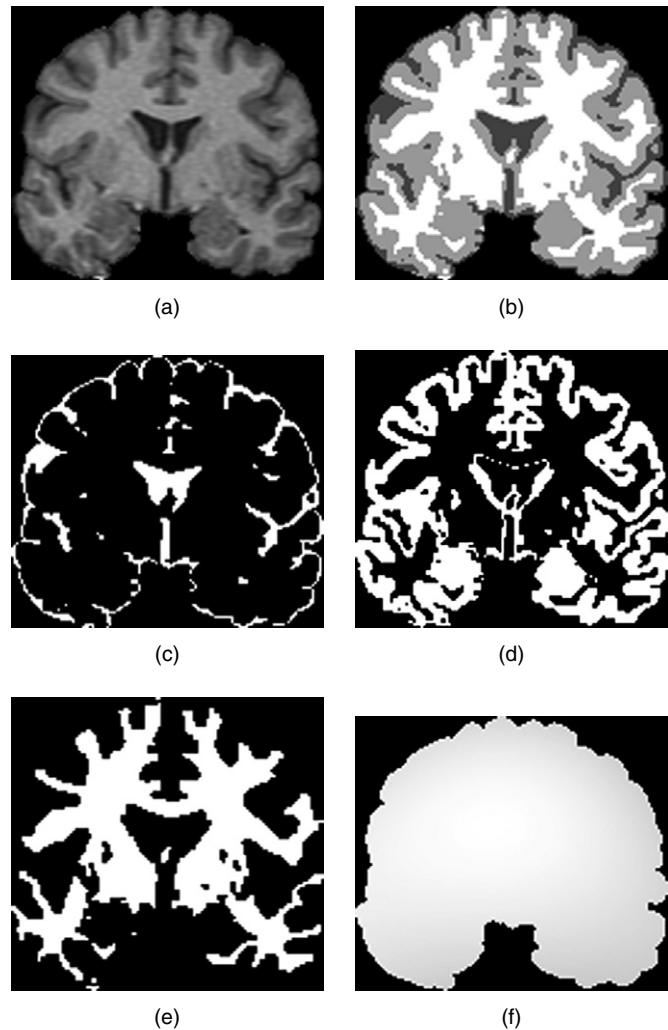


FIGURE 12.1 Robust K -means example: (a) T1-weighted MR image, (b) final classification, (c) CSF indicator function, (d) GM indicator function, (e) WM indicator function, (f) estimated inhomogeneity field.

12.3.2 EM Approach

A disadvantage of the K -means approach is that it directly estimates the binary indicator functions and therefore does not permit modeling of any uncertainty within the classification. An alternative approach to the optimization of Equation 12.6 is to use an EM algorithm [52]. The EM algorithm places the estimation problem within a complete/incomplete data framework and utilizes two main steps, the Expectation step (E-step) and the Maximization step (M-step), to optimize the cost function. In the case of the model described in Equation 12.2, the E-step computes a conditional expectation of the indicator function, yielding the posterior probability of each pixel belonging to a tissue class given the data. Although Equation 12.2 is an idealized case that does not explicitly account for partial volume effects, the posterior probabilities computed by the algorithm

are no longer binary and can be used as a measure of partial volume effects. The M-step consists of estimating the mean, variance, and gain field parameters.

Using the EM approach results in several differences from the K -means approach. The full derivation is similar to that presented in [12, 47] and is omitted here. First, the classification step of Equation 12.7 is replaced by the E-step. Because of the Markov random field assumption, a mean-field approximation [53] is used to estimate the posterior probabilities $w_{jk} = P(z_{jk} = 1 | \mathbf{y}; \theta)$. The resulting equation is

$$w_{jk} = \frac{\exp(-(y_j - g_j v_k)^2 / 2\sigma^2 - \beta \sum_{i \in N_j} \sum_{m \neq k} w_{jm})}{\sum_{l=1}^K \exp(-(y_j - g_j v_l)^2 / 2\sigma^2 - \beta \sum_{i \in N_j} \sum_{m \neq l} w_{jm})}. \quad (12.10)$$

Because the variance parameter now plays an important role in the E-step, it must be estimated during the parameter estimation step [47] using the following equation:

$$\sigma^2 = \frac{1}{N} \sum_{j \in \Omega} \sum_{k=1}^K w_{jk} (y_j - g_j v_k)^2. \quad (12.11)$$

The equations for estimating the class means and gain field are nearly identical to the K -means equations. The difference lies simply in replacing the indicator functions z_{jk} with the posterior probabilities w_{jk} .

Figure 12.2 shows the results of applying this robust EM algorithm to the same MR image described in Section 12.3.1. Unlike the K -means algorithm, the EM algorithm generates continuously valued indicators of each class rather than binary indicator functions, as shown in Figures 12.2c–e. The final classification, shown in Figure 12.2b, was created by assigning each pixel to the class associated with the highest probability at that location. Not surprisingly, the overall classification is quite similar to the K -means approach, since both algorithms are derived from the same objective function.

Note that one can interpret this algorithm as a noise-robust, inhomogeneity-adaptive version of clustering using finite Gaussian mixture models (FGMM) [52, 54]. A finite mixture model assumes that the image is composed of a mixture of observations sampled from K different probability densities $f_k(\mathbf{y}; \theta_k)$. Each observation has a probability α_k of being drawn from density k . The probability density function of a finite mixture model is given by

$$f(\mathbf{y}; \theta) = \sum_{k=1}^K \alpha_k f_k(\mathbf{y}; \theta_k). \quad (12.12)$$

The variables α_k are called *mixing coefficients* or *prior probabilities*. In the case of an FGMM, each f_k is Gaussian, parameterized by a mean and variance. The model described in this chapter is equivalent to the FGMM where the means and

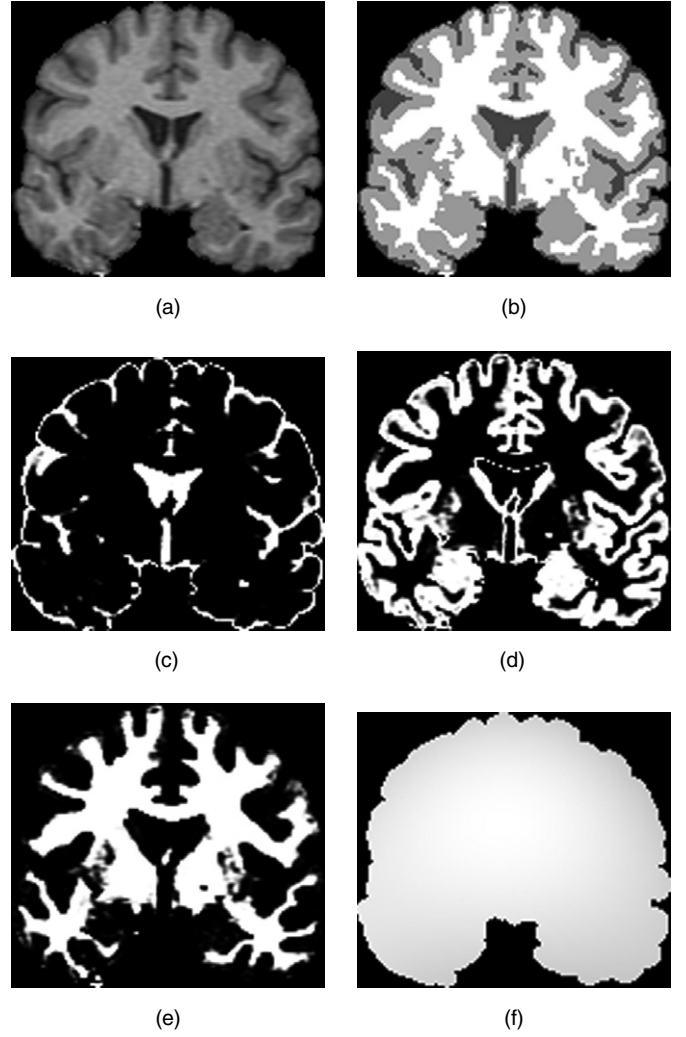


FIGURE 12.2 Robust EM algorithm example: (a) T1-weighted MR image, (b) final classification, (c) CSF posterior probability function, (d) GM posterior probability function, (e) WM posterior probability function, (f) estimated inhomogeneity field.

variances are equal for each class [47]. It is possible to allow these parameters to vary according to different classes while incorporating the gain field estimation and Markov random field prior. In theory, this should permit the model to possess greater flexibility and allow particular classes to exhibit greater intensity variations than others. However, in Section 12.4, it is shown that for the segmentation of single channel MR images, the equal mixing coefficients and variances model typically perform more accurately.

12.3.3 Fuzzy Clustering Approach

Another alternative to extending the K -means algorithm to provide soft segmentations is to use a fuzzy clustering approach. This leads to a robust version of the fuzzy K -means algorithm

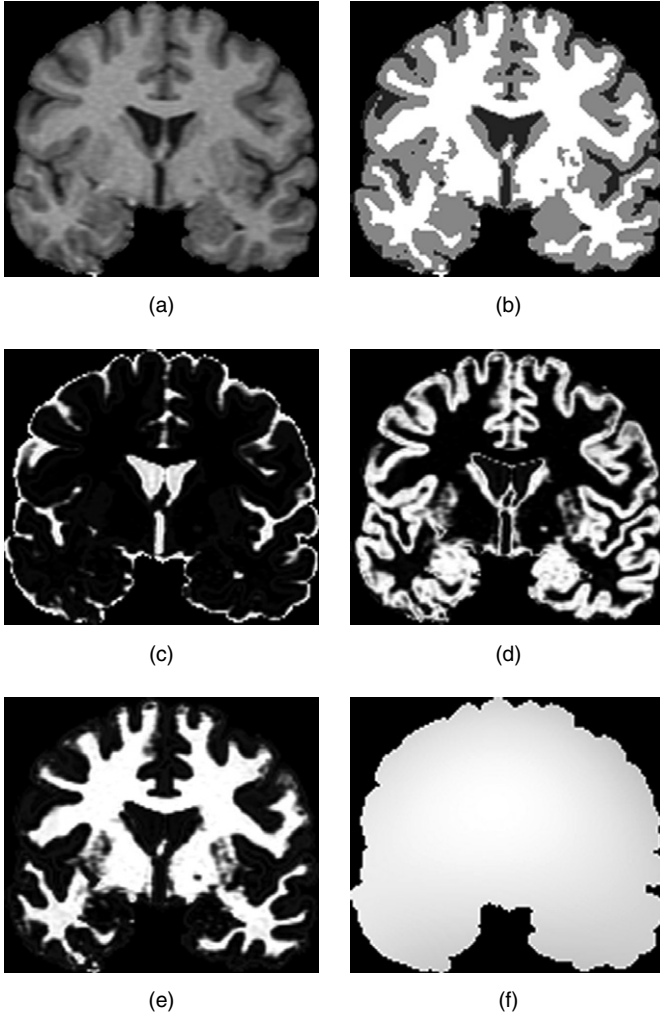


FIGURE 12.3 Robust fuzzy clustering example: (a) T1-weighted MR image, (b) final classification, (c) CSF membership function, (d) GM membership function, (e) WM membership function, (f) estimated inhomogeneity field.

[55]. Although fuzzy clustering does not have an explicit statistical interpretation, it can be derived through a direct generalization of the energy equation, Equation 12.6, by allowing the indicator function to be continuously valued between 0 and 1, and placing an exponent parameter within the objective function [55, 56]. In this case, the following fuzzy clustering replacement for E_1 is obtained:

$$E_1^{(\text{FC})} = \sum_{j \in \Omega} \sum_{i=1}^K u_{jk}^q (y_j - g_j v_k)^2, \quad (12.13)$$

where u_{jk} are now called *membership functions*. When $q = 1$, it has been shown that the membership functions will behave like binary indicator functions [55]. As q increases, the membership functions become increasingly “fuzzy,” allowing for more

uncertainty in the final classification. A commonly used value of q is 2.

To enforce spatial continuity within the membership functions, the neighborhood interaction energy can be generalized in a similar manner [16]:

$$E_2^{(\text{FC})} = \sum_{j \in \Omega} \sum_{i \in N_j} (u_j^q)^T V u_i^q,$$

where $\mathbf{u}_j^q = [u_{j1}^q, \dots, u_{jK}^q]^T$. Using this new energy function, the classification step now becomes

$$u_{jk} = \frac{\left((y_j - g_j v_k)^2 + 2\beta \sum_{i \in N_j} \sum_{m \neq k} u_{im}^q \right)^{-1/(q-1)}}{\sum_{l=1}^K \left((y_j - g_j v_l)^2 + 2\beta \sum_{i \in N_j} \sum_{m \neq l} u_{im}^q \right)^{-1/(q-1)}}. \quad (12.14)$$

Note the similarities between Equation 12.14 and Equation 12.10, particularly for $q = 2$, where the fuzzy clustering version simply lacks the exponential and variance. The gain field and mean estimation for the fuzzy clustering approach can be obtained simply by substituting u_{jk}^q for z_{jk} within the K -means equations.

Figure 12.3 shows the results of the robust fuzzy clustering algorithm when applied to the same MR image previously described in Section 12.3.1. Although the overall classification, shown in Figure 12.3b, is quite similar to both the K -means and EM results, the membership functions, shown in Figures 12.3c–e, preserve more details from the original image than the indicator functions or posterior probabilities computed by the other approaches.

12.4 Results

In this section, the different approaches are compared using simulated and real MR images of the brain. All brain images were preprocessed to remove extracranial tissue. For the K -means approaches, convergence was assumed to occur when less than 0.01% of pixels changed their classification between iterations. For all other algorithms, convergence was assumed to occur when the maximum change in the posterior probability or membership functions was less than 0.01 between iterations.

All three algorithms were implemented in Java as a plug-in for the Medical Image Processing, Analysis, and Visualization (MIPAV) software package [57]. Developed at the National Institutes of Health, MIPAV enables quantitative analysis and visualization of medical images from multiple modalities such as PET, MRI, CT, and microscopy. It includes basic and advanced computational methods to analyze and quantify biomedical data, supports all major medical image formats, and provides many visualization and data manipulation tools.

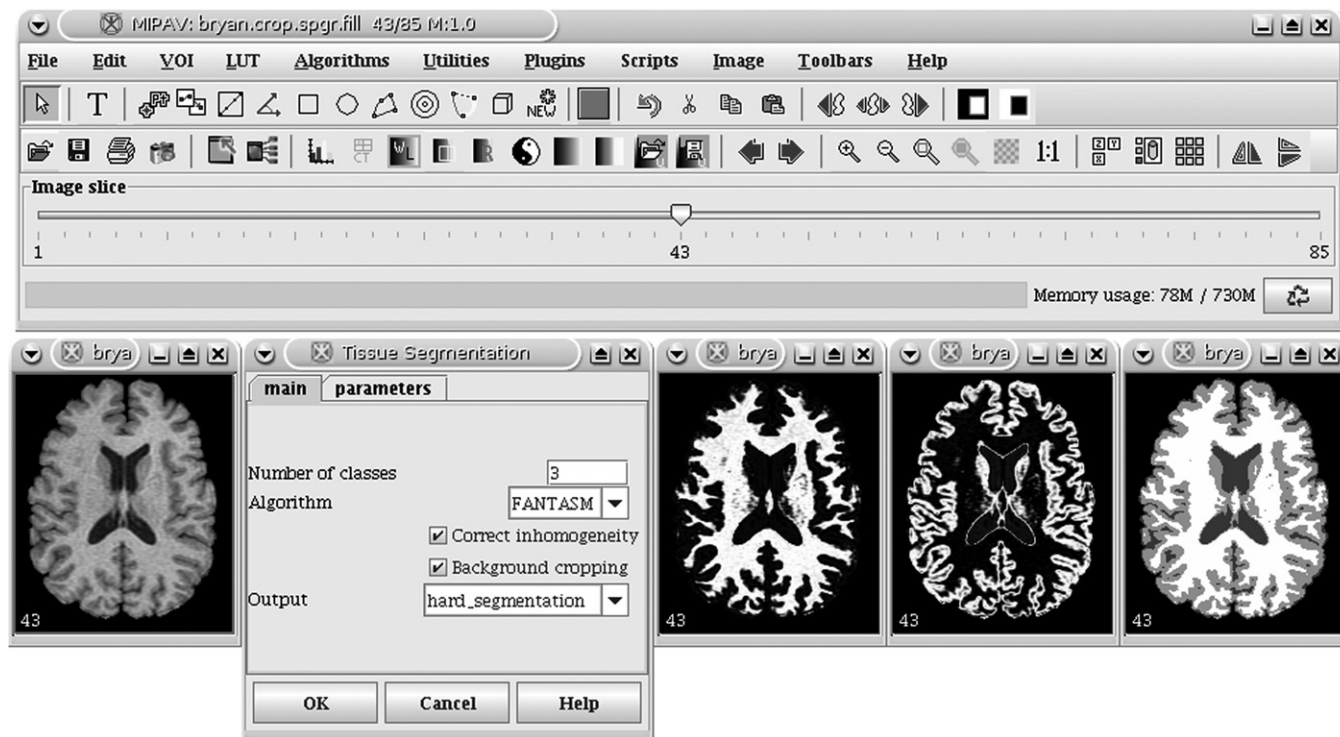


FIGURE 12.4 The MIPAV graphical user interface running the freely available Tissue Segmentation plug-in.

Because MIPAV is Java-based, it can be utilized on nearly any operating system, such as Windows, Unix, Linux, and Mac OS. MIPAV also provides an intuitive graphical user interface, providing researchers a user-friendly tool to visualize and analyze their imaging data. The entire MIPAV software package and documentation is freely downloadable from the Internet (<http://mipav.cit.nih.gov>).

Figure 12.4 shows the MIPAV interface running the Tissue Segmentation plug-in. The plug-in allows selection of one of five basic algorithms: the K -means approach; the EM approach; the fuzzy clustering approach (called FANTASM [58]); the EM approach, where the variances of each class are estimated separately; and the EM approach, where both the variances and mixing coefficients of each class are estimated separately. The user has the option to enable inhomogeneity correction and, under the parameter tab, may also specify smoothness, stopping criteria, and other more advanced settings. Thus, the standard versions of each of these approaches may be selected by disabling inhomogeneity correction and setting the smoothing parameter to 0. Execution times on a 3 GHz Pentium IV workstation running Linux vary depending on the parameter settings and dataset but were typically less than 90 seconds for both the robust K -means and fuzzy clustering approaches, and 3–5 minutes for the robust EM approach. Like MIPAV, the Tissue Segmentation plug-in is also freely downloadable from the Internet (<http://medic.rad.jhu.edu>).

12.4.1 Brainweb Dataset

The different variants of the classification algorithms were validated using the Brainweb simulated brain phantom [59] (<http://www.bic.mni.mcgill.ca/brainweb/>). The T1-weighted images were used with cubic voxel resolution and varying levels of noise and intensity inhomogeneity. Because the images are simulated, a truth model for both the classification and partial volumes within the images is available to compare against computed segmentations.

Figure 12.5 shows the results of applying the robust K -means (KM), robust EM, and robust fuzzy clustering (FC) algorithms to the Brainweb phantom with 3% noise and 40% inhomogeneity. All three approaches generate classifications that are visually quite comparable and are close to the true classification. In terms of estimating partial volumes, the membership function computed by the robust FC algorithm most closely resembles the truth model.

Table 12.1 shows the results of applying the different algorithms to the Brainweb phantom. The different columns represent the phantom simulated with different levels of noise (%N) and inhomogeneity (%I). The rows of the table represent the different methods, where an “R” denotes the robust version of the algorithm with inhomogeneity correction and smoothness constraints. “EMV” denotes the EM algorithm where a separate variance is estimated for each tissue class, and “EMPV” denotes where both separate mixing coefficients and variances

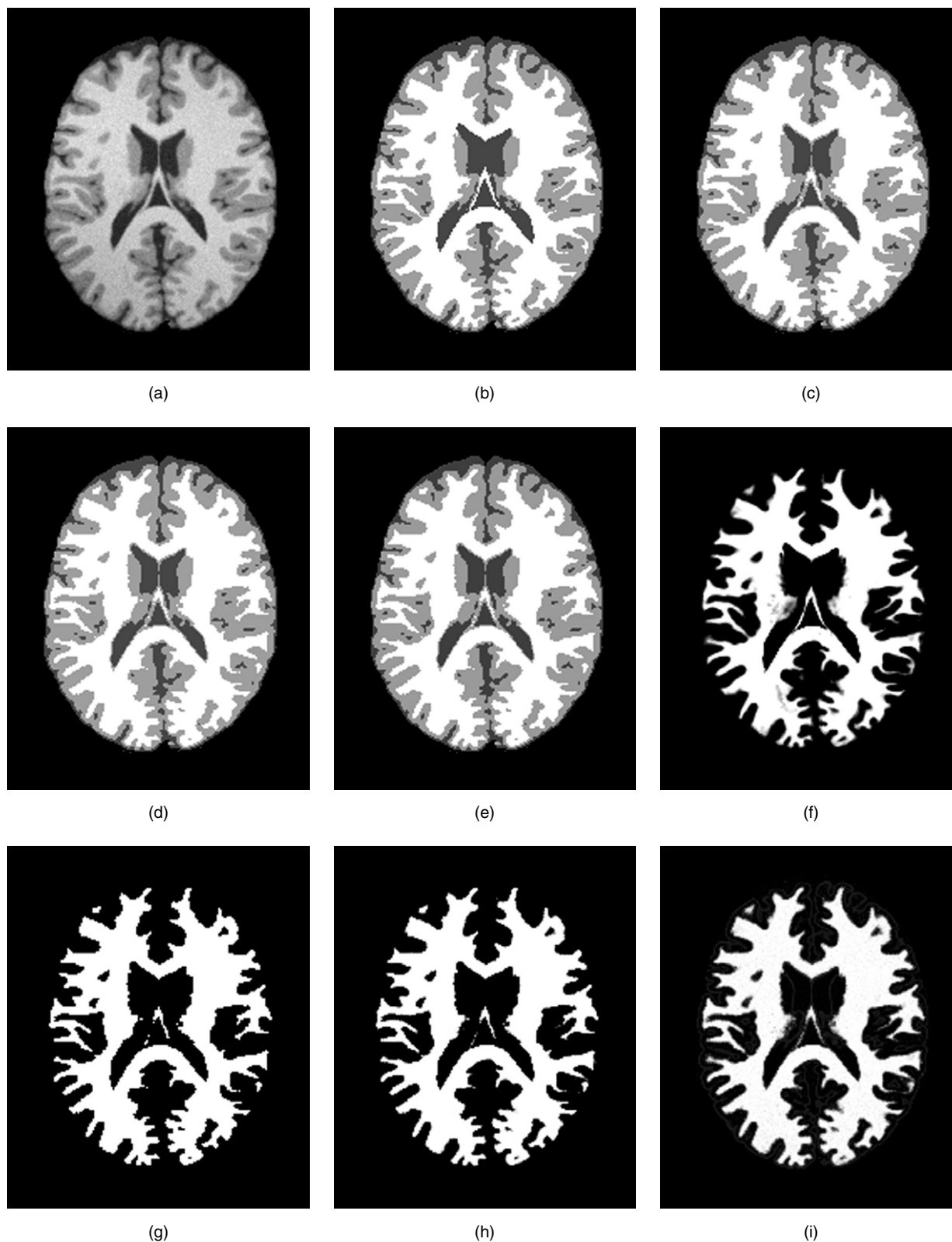


FIGURE 12.5 Robust tissue classification algorithms applied to the Brainweb phantom: (a) one slice of simulated image, (b) true classification, (c) robust KM classification, (d) robust EM classification, (e) robust FC classification, (f) true WM partial volumes, (g) robust K -means indicator function, (h) robust EM posterior probability function, (i) robust FC membership function.

TABLE 12.1 Brainweb classification errors (MCR is the percentage of misclassified pixels; RMS is the root mean squared difference between the true partial volume and the algorithm estimate).

Method	3%N, 0%I	3%N, 20%I	3%N, 40%I	5%N, 0%I	5%N, 20%I	5%N, 40%I	7%N, 20%I
KM-MCR	4.17%	5.57%	9.20%	6.72%	7.68%	11.04%	10.61%
KM-RMS	0.24	0.25	0.30	0.27	0.28	0.32	0.31
RKM-MCR	4.26%	4.21%	4.19%	5.70%	5.57%	5.46%	7.52%
RKM-RMS	0.24	0.24	0.23	0.25	0.25	0.25	0.28
EM-MCR	4.33%	5.73%	9.47%	7.12%	7.98%	11.44%	11.31%
EM-RMS	0.18	0.19	0.22	0.20	0.21	0.24	0.24
EMV-MCR	8.66%	9.81%	14.46%	10.59%	11.54%	15.95%	15.15%
EMV-RMS	0.25	0.25	0.28	0.26	0.26	0.29	0.29
EMPV-MCR	5.43%	6.95%	13.02%	6.54%	7.72%	10.87%	10.68%
EMPV-RMS	0.19	0.21	0.28	0.20	0.21	0.24	0.24
REM-MCR	4.26%	4.21%	4.19%	5.70%	5.57%	5.46%	7.52%
REM-RMS	0.20	0.20	0.20	0.21	0.21	0.21	0.22
FC-MCR	4.11%	5.51%	9.08%	6.70%	7.61%	10.87%	10.73%
FC-RMS	0.13	0.15	0.21	0.18	0.19	0.23	0.23
RFC-MCR	4.14%	4.10%	4.17%	5.55%	5.43%	5.39%	7.27%
RFC-RMS	0.13	0.12	0.13	0.15	0.15	0.15	0.17

are estimated. Two different measures were computed based on the results. The misclassification rate (MCR) was computed as

$$\text{MCR} = \frac{\text{number of pixels misclassified}}{\text{total number of pixels}}.$$

Background pixels were ignored in the MCR computation. The other measure used was the root mean squared (RMS) difference between the indicator, posterior probability, or membership function and the true partial volumes. The RMS error was averaged over all three tissue classes. The smoothing parameters were set to 0.03, 0.05, and 6.0 for the RKM, RFC, and REM algorithms, respectively.

All algorithms have increasing errors with increasing levels of noise. However, the robust algorithms are affected substantially less than the standard algorithms. Furthermore, increasing inhomogeneity greatly affects the standard algorithms, but the estimation of the gain field within the robust algorithms fully compensates for the artifact. The three robust algorithms produced similar misclassification rates but, as indicated in Figure 12.5, the fuzzy clustering approaches produce the lowest RMS error.

Note also that the simplest model of the different EM algorithm variations performed the best overall. To illustrate the differences, the results of EM, EMV, and EMPV are shown in Figure 12.6 when applied to the phantom with 3% noise and 0% inhomogeneity. The model where separate variances are estimated for each class (EMV) overestimated CSF, while the model with separate variances and mixing coefficients (EMPV) produced an excess of gray matter.

12.4.2 IBSR Datasets

The different robust algorithms were applied to 18 volumetric T1-weighted MR datasets with expert segmentations obtained from the Internet Brain Segmentation Repository (available from <http://www.cma.mgh.harvard.edu/ibsr/>). Figure 12.7 shows the results of applying the robust fuzzy clustering algorithm to image 2 of the IBSR dataset. Figure 12.8 plots the resulting Dice coefficient computed from the classifications of the three robust algorithms on each dataset. The Dice coefficient is a value between 0 and 1 and defined as

$$\text{Dice} = \frac{2|S \cap T|}{|S| + |T|}$$

where S is the set of pixels corresponding to the estimated tissue class, T is the set of pixels corresponding to the true class, and $|\cdot|$ denotes the number of pixels in the class. The CSF results are not shown but are generally low (averaging around 0.13), since the expert segmentations have very small levels of sulcal CSF. Overall, the performance of all three algorithms was very similar.

12.4.3 Sensitivity to Scan Protocol

Even though the described methods are unsupervised, they are still sensitive to the contrast properties of the scan protocol. Figure 12.9 shows the results of the robust fuzzy clustering classification for two different T1-weighted scans acquired from the same subject. One scan is an SPGR acquired on a GE

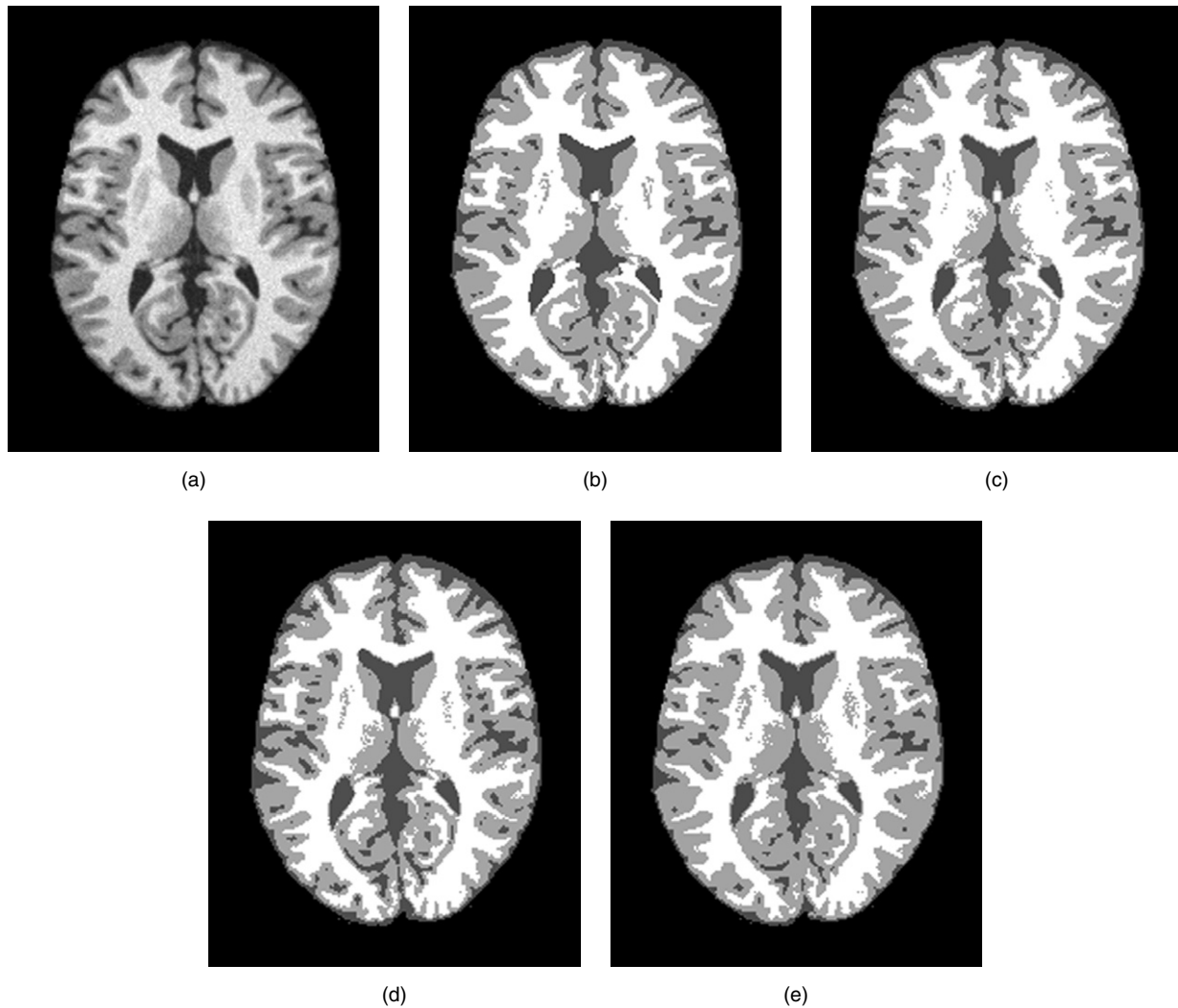


FIGURE 12.6 Comparison of EM algorithms applied to the Brainweb phantom: (a) one slice of original image, (b) true classification, (c) EM with equal mixing coefficients and variances, (d) EM with separate variances, (e) EM with separate variances and mixing coefficients.

scanner, shown in Figure 12.9a, and the other is a Magnetization Prepared Rapid Gradient Echo (MPRAGE) acquired on a Philips scanner. Approximately the same slice is shown from the subject. Although both images are T1-weighted, they have different characteristics, thereby resulting in substantially different classifications. The MPRAGE classification shows increased sulcal CSF, decreased cortical thickness, and increased subcortical gray matter, relative to the SPGR.

12.5 Conclusions

From a fairly simple statistical image model, three different algorithms were derived for obtaining noise and inhomogeneity robust tissue classifications. The algorithms generalize the standard pattern recognition techniques of K -means clustering, fuzzy clustering, and Gaussian clustering with the EM

algorithm. Because they are derived from the same model, the classification results from each are quite similar. However, the fuzzy clustering approach produces better modeling of partial volume effects. If only a classification is required, then the K -means algorithm may be preferable to the EM approach, since it is computationally faster. The more flexible EM models that allow separate variances and mixing coefficients for each class surprisingly did not produce as accurate segmentations as the simpler model in these validation studies. This may be because these models have greater degrees of freedom and are more susceptible to local optima. Care must be taken when applying these algorithms to datasets consisting of scans from different scanners or protocols, since contrast changes in the images may significantly alter the classification results. Further extensions of these algorithms to incorporate spatial priors and other constraints would likely ameliorate this issue.

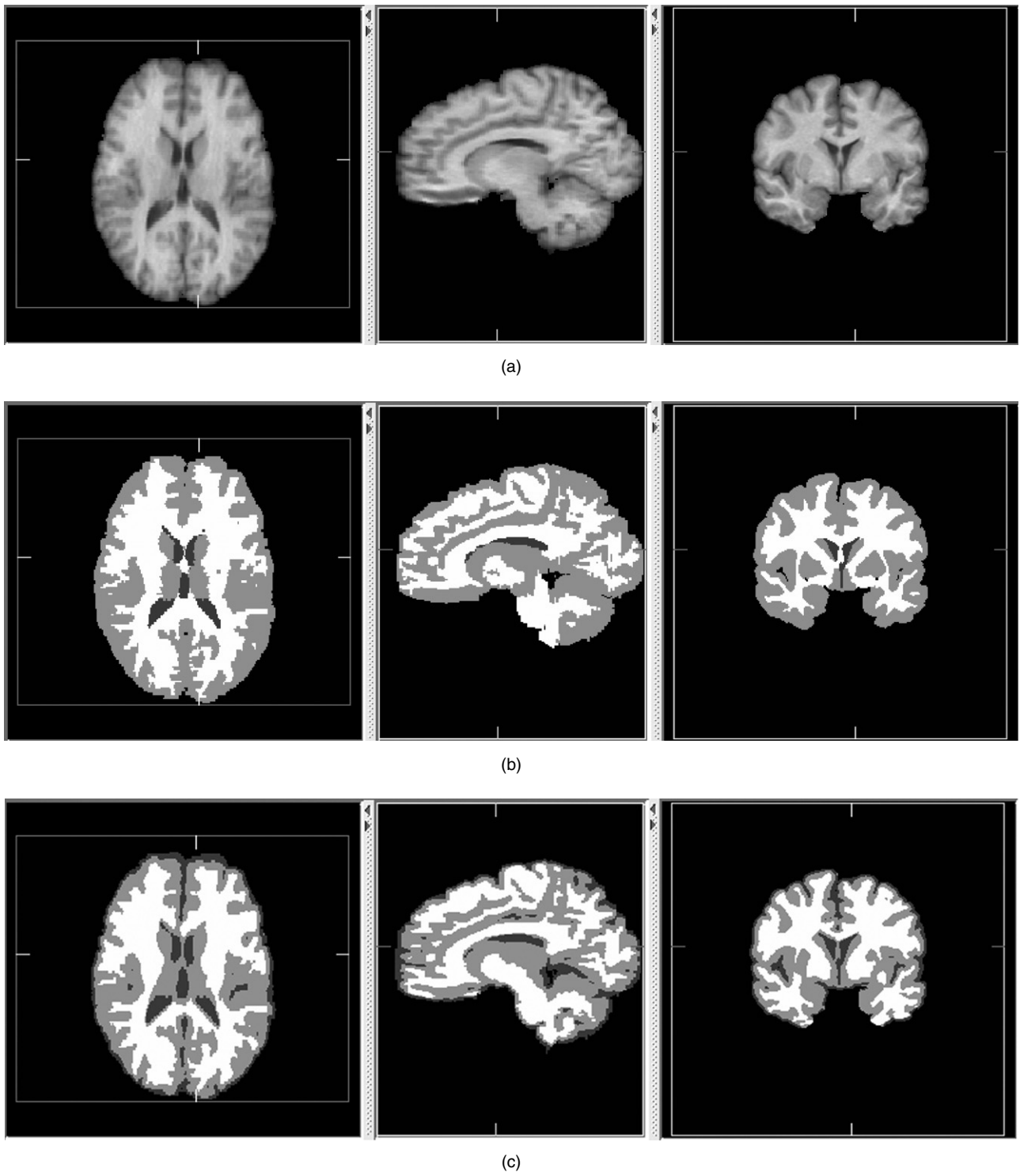


FIGURE 12.7 IBSR dataset: (a) Triplanar view of a dataset, (b) expert classification, (c) robust fuzzy clustering classification.

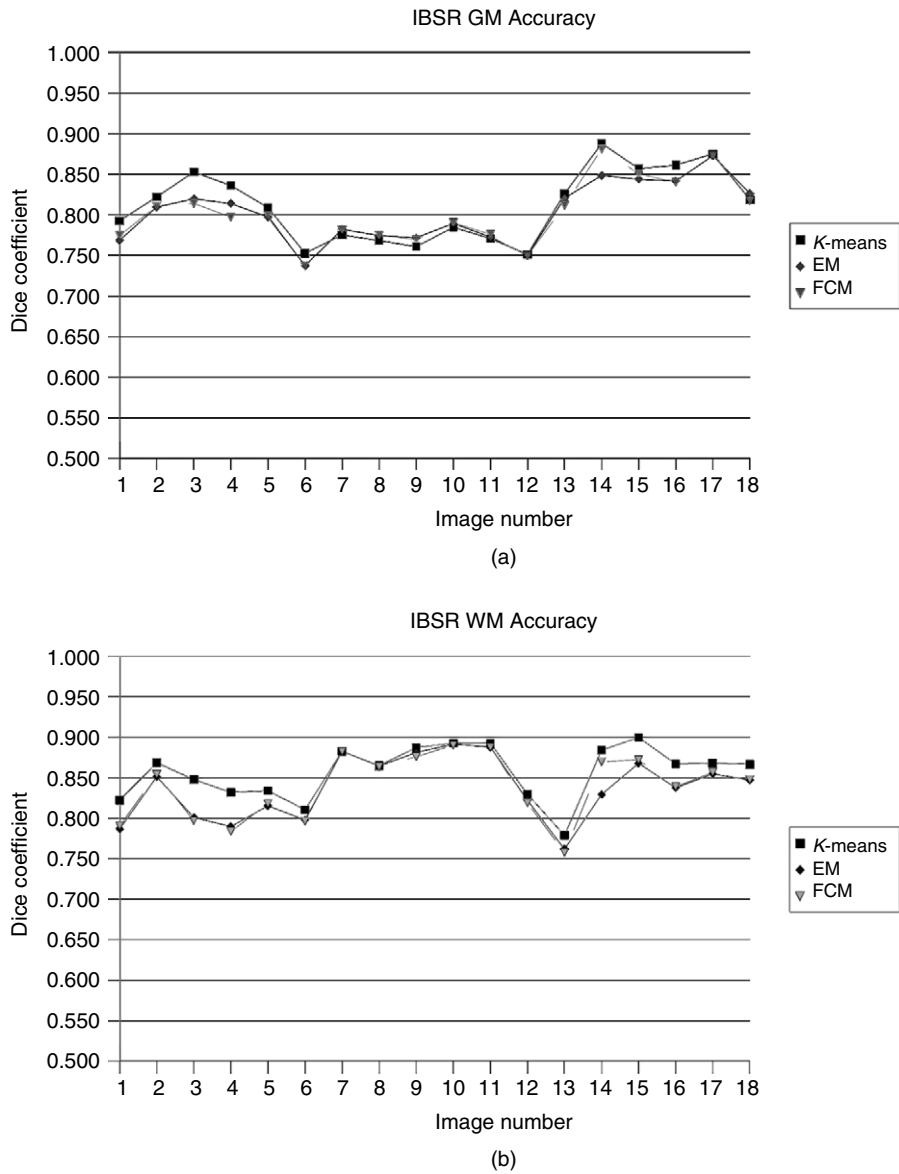


FIGURE 12.8 Robust tissue classification algorithms applied to IBSR data: (a) Dice coefficients for gray matter, (b) Dice coefficients for white matter.

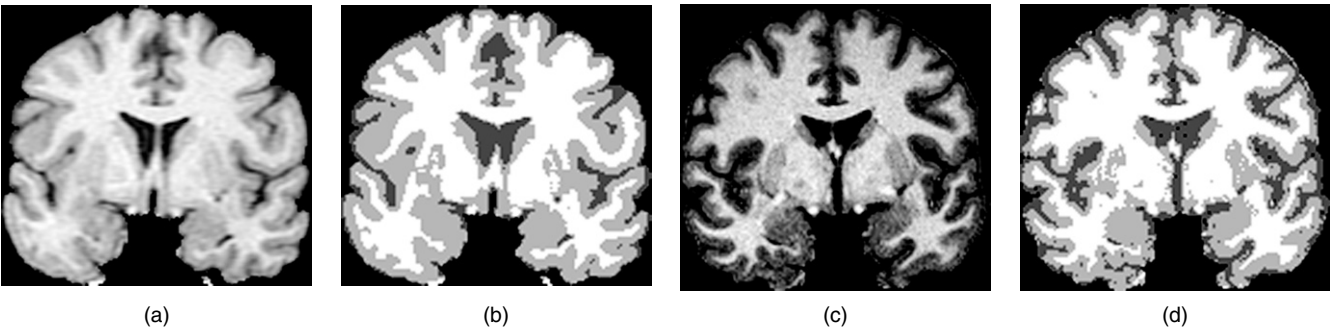


FIGURE 12.9 Approximately the same slice from the same subject acquired with two different scan protocols: (a) SPGR scan, (b) robust fuzzy clustering classification of SPGR scan, (c) MPRAGE scan, (d) robust fuzzy clustering classification of MPRAGE scan.

12.6 References

1. Pham DL, Xu C, Prince JL. Current methods in medical image segmentation. *Annual Review of Biomedical Engineering*. 2000;2:315–337.
2. Sled JG, Pike GB. Standing-wave and RF penetration artifacts caused by elliptic geometry: An electrodynamic analysis of MRI. *IEEE Trans on Medical Imaging*. 1998;17: 653–662.
3. Santago P, Gage HD. Statistical models of partial volume effect. *IEEE Trans Image Processing*. 1995;4:1531–1540.
4. Duda RO, Hart PE, Stork DG. *Pattern Classification*, 2nd ed. Wiley-Interscience: 2000.
5. Bezdek JC, Hall LO, Clarke LP. Review of MR image segmentation techniques using pattern recognition. *Medical Physics*. 1993;20:1033–1048.
6. Li SZ. *Markov Random Field Modeling in Computer Vision*. Springer; 1995.
7. Held K, Kops ER, Krause BJ, Wells WM, Kikinis R, Muller-Gartner H. Markov random field segmentation of brain MR images. *IEEE Trans on Medical Imaging*. 1997;16(6): 878–886.
8. Kapur T, Grimson WEL, Kikinis R, Wells WM. Enhanced spatial priors for segmentation of magnetic resonance imagery. In *Proc of the First Int Conf on Medical Image Computing and Computer Assisted Interventions (MICCAI98)*. 1998;457–468.
9. Pappas TN. An adaptive clustering algorithm for image segmentation. *IEEE Trans on Signal Processing*. 1992;40: 901–914.
10. Rajapakse JC, Giedd JN, Rapoport JL. Statistical approach to segmentation of single-channel cerebral MR images. *IEEE Trans on Medical Imaging*. 1997;16:176–186.
11. Leemput KV, Maes F, Vandermulen D, Seutens P. Automated model-based tissue classification of MR images of the brain. *IEEE Trans on Medical Imaging*. 1999;18(10):897–908.
12. Pham DL, Prince JL. A generalized EM algorithm for robust segmentation of magnetic resonance images. In *Proceedings of the 33rd Annual Conference on Information Sciences and Systems (CISS99)*. Johns Hopkins University; 1999.
13. Zhang Y, Brady M, Smith S. Segmentation of brain MR images through a hidden Markov random field model and the expectation-maximization algorithm. *IEEE Trans on Medical Imaging*. 2001;20(1):45–57; see <http://www.fmrib.ox.ac.uk/fsl/fast/index.html>.
14. Marroquin JL, Vemuri BC, Botello S, Calderon F, Fernandez-Bouzas A. An accurate and efficient Bayesian method for automatic segmentation of brain MRI. *IEEE Trans on Medical Imaging*. 2002;21(8):934–945.
15. Marroquin JL, Santana EA, Botello S. Hidden Markov measure field models for image segmentation. *IEEE Trans on Pattern Anal Machine Intell*. 2003;25(11):1380–1387.
16. Pham DL. Spatial models for fuzzy clustering. *Computer Vision and Image Understanding*. 2001;84(2):285–297.
17. Liew AWC, Leung SH, Lau WH. Fuzzy image clustering incorporating spatial continuity. *IEE Proc—Vis Image Signal Process*. 2000;147(2):185–192.
18. Ahmed MN, Yamany SM, Mohamed N, Farag AA, Moriarty T. A modified fuzzy c-means algorithm for bias field estimation and segmentation of MRI data. *IEEE Transactions on Medical Imaging*. 2002;21:193–199.
19. Lim KO, Pfefferbaum A. Segmentation of MR brain images into cerebrospinal fluid and white and gray matter. *Journal of Computer Assisted Tomography*. 1989;13:588–593.
20. Dawant BM, Zijdenbos AP, Margolin RA. Correction of intensity variations in MR images for computer-aided tissue classification. *IEEE Trans on Medical Imaging*. 1993;12:770–781.
21. Meyer CR, Peyton HB, Pipe J. Retrospective correction of intensity inhomogeneities in MRI. *IEEE Trans on Medical Imaging*. 1995;14:36–41.
22. Johnston B, Atkins MS, Mackiewicz B, Anderson M. Segmentation of multiple sclerosis lesions in intensity corrected multispectral MRI. *IEEE Trans on Medical Imaging*. 1996;15:154–169.
23. Lee SK, Vannier MW. Post-acquisition correction of MR inhomogeneities. *Magnetic Resonance in Medicine*. 1996;36:276–286.
24. Brinkmann BH, Manduca A, Robb RA. Optimized homomorphic unsharp masking for MR grayscale inhomogeneity correction. *IEEE Trans on Medical Imaging*. 1998;17:161–171.
25. Sled JG, Zijdenbos AP, Evans AC. A nonparametric method for automatic correction of intensity nonuniformity in MRI data. *IEEE Trans on Medical Imaging*. 1998;17:87–97.
26. Shattuck DW, Sandor-Leahy SR, Schaper KA, Rottenberg DA, Leahy RM. Magnetic resonance image tissue classification using a partial volume model. *Neuroimage*. 2001;13:856–876.
27. Unser M. Multigrid adaptive image processing. In *Proc of the IEEE Conference on Image Processing (ICIP95)*. 1995; I:49–52.
28. Rajapakse JC, Kruggel F. Segmentation of MR images with intensity inhomogeneities. *Image and Vision Computing*. 1998;16:165–180.
29. Wells WM, Grimson WEL, Kikinis R, Jolesz FA. Adaptive segmentation of MRI data. *IEEE Trans on Medical Imaging*. 1996;15:429–442.
30. Pham DL, Prince JL. Adaptive fuzzy segmentation of magnetic resonance images. *IEEE Trans on Medical Imaging*. 1999;18(9):737–752.
31. Santago P, Gage HD. Quantification of MR brain images by mixture density and partial volume modeling. *IEEE Trans Medical Imaging*. 1993;12:566–574.

32. Tohka J, Zijdenbos A, Evans A. Fast and robust parameter estimation for statistical partial volume models in brain MRI. *Neuroimage*. 2004;23(1):84–97.
33. Choi HS, Hanynor DR, Kim Y. Partial volume tissue classification of multichannel magnetic resonance images—A mixel model. *IEEE Trans on Medical Imaging*. 1991;10:395–407.
34. Soltanian-Zadeh H, Windham JP, Yagle AE. Optimal transformation for correcting partial volume averaging effects in magnetic resonance imaging. *IEEE Transactions on Nuclear Science*. 1993;40(4):1204–1212.
35. Laidlaw DH, Fleischer KW, Barr AH. Partial-volume Bayesian classification of material mixtures in MR volume data using voxel histograms. *IEEE Transactions on Medical Imaging*. 1998;17:74–86.
36. Niessen WJ, Vincken KL, Weickert J, Ter Haar Romeny BM, Viergever MA. Multiscale segmentation of three-dimensional MR brain images. *International Journal of Computer Vision*. 1999;31(2–3):185–202.
37. Van Leemput K, Maes F, Vandermeulen D, Suetens P. A unifying framework for partial volume segmentation of brain MR images. *IEEE Transactions on Medical Imaging*. 2003;22:105–119.
38. Ashburner J, Friston KJ. Unified segmentation. *Neuroimage*. 2005;26(3):839–851.
39. Fischl B, Salat DH, Busa E, Albert M, Dieterich M, Haselgrove C, van der Kouwe A, Killiany R, Kennedy D, Klaveness S, Montillo A, Makris N, Rosen B, Dale AM. Whole brain segmentation—Automated labeling of neuroanatomical structures in the human brain. *Neuron*. 2002;33:341–355.
40. Cocosco C, Zijdenbos A, Evans A. A fully automatic and robust brain MRI tissue classification method. *Medical Image Analysis*. 2003;7(4):513–27.
41. Pohl KM, Fisher J, Grimson WEL, Kikinis R, Wells WM. A Bayesian model for joint segmentation and registration. *Neuroimage*. 2006;31:228–39.
42. Pham DL, Bazin PL. Simultaneous registration and tissue classification using clustering algorithms. In *Proceedings of the 3rd IEEE International Symposium on Biomedical Imaging: Macro to Nano*. 2001:650–653.
43. Bazin PL, Pham DL. Topology preserving tissue classification with fast marching and topology templates. In *Proceedings of the 19th International Conference on Information Processing in Medical Imaging*. 2005:LNCS 3565:234–245.
44. Bazin PL, Pham DL. TOADS: Topology-preserving, anatomy-driven segmentation. In *Proceedings of the 3rd IEEE International Symposium on Biomedical Imaging: Macro to Nano*. 2006:327–330.
45. Bazin PL, Pham DL. Topology-preserving tissue classification of magnetic resonance brain images. *IEEE Trans on Medical Imaging*, forthcoming.
46. Van Leemput K, Maes F, Vandermeulen D, Colchester A, Suetens P. Automated segmentation of multiple sclerosis lesions by model outlier detection. *IEEE Trans on Medical Imaging*. 2001;20(8):677–688.
47. Pham DL. *Statistical Estimation and Pattern Recognition Methods for Robust Segmentation of Magnetic Resonance Images*. Ph.D. thesis, Johns Hopkins University; 1999.
48. Pham DL, Prince JL. Robust unsupervised tissue classification in MR images. In *Proceedings of the 2004 IEEE International Symposium on Biomedical Imaging: Macro to Nano*. 2004:109–112.
49. Besag J. On the statistical analysis of dirty pictures. *CVGIP: Image Understanding*. 1986;57:359–372.
50. Davis PJ. *Interpolation and Approximation*. Dover; 1975.
51. Pham DL, Prince JL. An adaptive fuzzy c-means algorithm for image segmentation in the presence of intensity inhomogeneities. *Pattern Recognition Letters*. 1999;20:57–68.
52. Dempster AP, Laird NM, Rubin DB. Maximum likelihood from incomplete data via the EM algorithm. *Journal of the Royal Statistical Society Series B*. 1977;39:1–38.
53. Zhang J. The mean field theory in EM procedures for Markov random fields. *IEEE Trans on Signal Processing*. 1992;40:2570–2583.
54. Redner RA, Walker HF. Mixture densities, maximum likelihood and the EM algorithm. *SIAM Review*. 1984;26(2):197–237.
55. Bezdek JC. A convergence theorem for the fuzzy ISODATA clustering algorithms. *IEEE Trans on Pattern Anal Machine Intell*. 1980;PAMI-2:1–8.
56. Dunn JC. A fuzzy relative of the ISODATA process and its use in detecting compact well-separated clusters. *Journal of Cybernetics*. 1973;3:32–57.
57. McAuliffe MJ, Lalonde F, McGarry DP, Gandler W, Csaky K, Trus BL. Medical image processing, analysis and visualization in clinical research. In *Proceedings of the 14th IEEE Symposium on Computer-Based Medical Systems (CBMS 2001)*. 2001:381–386.
58. Han X, Pham DL, Tosun D, Rettmann ME, Xu C, Prince JL. CRUISE: Cortical reconstruction using implicit surface evolution. *Neuroimage*. 2004;23(3):997–1012.
59. Collins DL, Zijdenbos AP, Kollokian V, Sled JG, Kabani, NJ, Holmes CJ, Evans AC. Design and construction of a realistic digital brain phantom. *IEEE Trans on Medical Imaging*. 1998;17:463–468.